A new non-linear RANS model with enhanced near-wall treatment of turbulence anisotropy

Fadhila, H. N., Medina, H., Aleksandrova, S. & Benjamin, S.

Original citation & hyperlink:
Fadhila, HN, Medina, H, Aleksandrova, S & Benjamin, S 2020, 'A new non-linear RANS model with enhanced near-wall treatment of turbulence anisotropy', Applied Mathematical Modelling, vol. 82, pp. 293-313.
https://dx.doi.org/10.1016/j.apm.2020.01.056

DOI 10.1016/j.apm.2020.01.056
ISSN 0307-904X

Publisher: Elsevier

A new non-linear RANS model with enhanced near-wall treatment of turbulence anisotropy

H. Fadhila[a,*], H. Medina[a], S. Aleksandrova[a], S. Benjamin[a]

[a]*Coventry University, Faculty of Engineering, Environment & Computing, Coventry, United Kingdom*

Abstract

A new ω-based non-linear eddy-viscosity model is proposed. It was developed based on the original $k-\omega$ model and formulated using a quadratic stress-strain relation for the Reynolds stress tensor, with an added realisability condition. For enhanced treatment of near-wall turbulence anisotropy, a formulation that scales only with the turbulent Reynolds number is proposed for the first time. The new model has been implemented in the open-source Computational Fluid Dynamics (CFD) package OpenFOAM and validated against plane channel flow, a zero-pressure-gradient flat plate, and a U-bend curved channel configuration. To further assess the performance of the model for more complex geometries, it has been tested on configurations relevant to automotive applications. Overall, the new model outperforms the standard $k-\omega$ model. For example, on a curved channel, improved predictions for the minimum pressure and maximum skin friction of approximately 50% are obtained. Improved predictions are also obtained for quantities of practical engineering relevance, such as the pressure distribution along the wall of a sudden expansion diffuser, a configuration used to inform the design of automotive exhaust systems. This demonstrates that the proposed model has important practical applications for internal flows where anisotropic turbulence effects dominate.

Keywords: turbulence, anisotropy, near-wall, OpenFOAM, diffuser, swirling flow

1. Introduction

Turbulence modelling is an attempt to predict the chaotic and anisotropic turbulent behaviour which is found in many practical flows that involve features such as curvature, boundary layer transition, impingement, separation, or swirling. Despite the growth in computing power in the recent years and the continuing development in the performance and applicability of Direct Numerical Simulation (DNS) and Large-Eddy Simulation (LES), Reynolds-averaged Navier-Stokes (RANS) models continue to be the cornerstone of turbulence modelling for complex engineering flows due to the inevitable compromise between accuracy and cost. The RANS equations can be used to find steady-state solutions of the flow field where the influence of turbulence is represented as a net loss of momentum by the Reynolds stress

*Corresponding author
Email address: fadhilah@uni.coventry.ac.uk (H. Fadhila)

Nomenclature

Acronyms

CFD	Computational Fluid Dynamics
DNS	Direct Numerical Simulation
EARSM	Explicit Algebraic Reynolds Stress Model
LES	Large-Eddy Simulation
NL	Non-Linear
RANS	Reynolds-Averaged Navier-Stokes
RSM	Reynolds Stress Model

Greek Symbols

δ_{ij}	Kronecker delta
ν	Laminar kinetic viscosity $[m^2/s]$
ν_T	Eddy viscosity $[m^2/s]$
Ω	Magnitude of vorticity rate tensor: $\sqrt{2\Omega_{ij}\Omega_{ij}}$ $[s^{-1}]$
ω	Specific dissipation rate $[s^{-1}]$
Ω_{ij}	Vorticity rate tensor: $\frac{1}{2}\left(\frac{\partial U_i}{\partial x_j} - \frac{\partial U_j}{\partial x_i}\right)$ $[s^{-1}]$
$\tilde{\Omega}$	Vorticity rate tensor invariant: $\frac{1}{\omega}\sqrt{2\Omega_{ij}\Omega_{ij}}$
ε	Dissipation rate $[m^2/s^3]$

Roman Symbols

$\overline{u_i'u_j'}$	Reynolds stress tensor $[m^2/s^2]$
$\tilde{S}$	Strain rate tensor invariant: $\frac{1}{\omega}\sqrt{2S_{ij}S_{ij}}$
a_{ij}	Anisotropy tensor
C_f	Skin friction coefficient: $\frac{\tau_w}{1/2\rho U_\infty^2}$
C_p	Pressure coefficient
k	Turbulent kinetic energy $[m^2/s^2]$
P_k	Production of k $[m^2/s^3]$
Re	Reynolds number: $\frac{U_\infty L}{\nu}$
Re_τ	Wall shear Reynolds number: $\frac{u_\tau L}{\nu}$
S	Magnitude of strain rate tensor: $\sqrt{2S_{ij}S_{ij}}$ $[s^{-1}]$
S_{ij}	Strain rate tensor: $\frac{1}{2}\left(\frac{\partial U_i}{\partial x_j} + \frac{\partial U_j}{\partial x_i}\right)$ $[s^{-1}]$
Tu	Turbulence intensity: u'/U_∞
U	Mean velocity $[m/s]$
$u_i'u_i'^+$	Dimensionless Reynolds stress components: $u_i'u_i'/u_\tau^2$
u_i'	Fluctuating velocity vector $[m/s]$
$u'v'$	Turbulent shear stress $[m^2/s^2]$
u'	Streamwise fluctuating velocity $[m/s]$
u_τ	Wall shear velocity $[m/s]$
v'	Wall-normal fluctuating velocity $[m/s]$
w'	Spanwise fluctuating velocity $[m/s]$
x	Streamwise coordinate $[m]$
y	Wall-normal distance $[m]$
y^+	Dimensionless wall-normal distance: $u_\tau y/\nu$

Subscripts

∞	Refers to freestream condition

tensor. This introduces additional unknown quantities and results in the 'closure problem' i.e. there are more unknown variables than equations. Turbulence models are used to close the system of equations by providing a means of estimating the Reynolds stress tensor.

The Boussinesq hypothesis is the most widely-used approach to model the turbulent

Reynolds stresses, in which a linear relation between the Reynolds stress tensor and the mean rate-of-strain is assumed. **This approach has been applied extensively in the academic and industrial communities over the past few decades, with relative success since as early as the 1970s–1980s in flow problems such as turbulent boundary layers [1, 2] and recirculating flows [3–6].** However, the Boussinesq approximation has been known to fail in many cases. Flows involving highly three-dimensional and anisotropic features cannot be represented accurately using this linear relation. Notable examples include the presence of secondary flows in non-circular ducts which arise from the anisotropic nature of the normal Reynolds stresses [7], the marked influence that wall-normal velocity fluctuations have on the structure of a boundary layer [8], the effects of streamline curvature on the asymmetric velocity profile in flows over curved sufaces [9, 10], the non-linear effects of imposed system rotation on turbulent flows [11], and the anisotropic velocity fluctuations in the stagnation region of an impinging jet [12].

Due to the well-known deficiencies of linear eddy-viscosity models, Schmitt [13] has used DNS, LES, and an experimental database to quantify the degree of validity of the Boussinesq proportionality assumption to a number of cases including simple shear flows, flow over a square cylinder, and a double annular turbulent jet flow. The results show consistently the limitations of this assumption. These limitations help to explain why in complex flows, e.g. ones in which high mixing rates and stagnation regions are present, the predictions of the mean flow fields by linear models can be inaccurate [14]. Even for simple cases, such as a simple shear flow, they have been known to incorrectly predict the Reynolds stress components due to their isotropic formulation [15–17]. Even though this is a simple case, the redistribution of the different Reynolds stress components has important effects when the model is used to capture complex features near the wall on more complex test cases [18, 19]. Durbin [19] also observed based on the DNS data of Kim et al. [20] that the near-wall damping of eddy viscosity is caused by the suppression of the wall-normal velocity fluctuation, $\overline{v'v'}$, which when modelled accurately as a velocity scale can be used to avoid the overprediction of turbulent viscosity near the wall, hence promoting separation [21]. This redistribution is also important for modelling of flows over curved surfaces, since in such cases a transfer of kinetic energy exists that leaves the total kinetic energy unchanged, but affects the distribution of the different fluctuating velocity components [22].

To achieve a more accurate modelling of the Reynolds stresses, one approach is to abandon the Boussinesq approximation and directly solve for all the individual components of the Reynolds stress tensor, a concept known as Reynolds Stress Modelling (RSM) [15, 23]. However, this approach results in the introduction of 6 additional highly-coupled, non-linear partial differential equations, which makes solving the problem difficult and costly. **Consequently, an approach to simplify the RSM concept is proposed by obtaining an implicit algebraic approximation to it under the weak-equilibrium assumption, as suggested by Rodi [24, 25].** However, this also poses some numerical and computational challenges, which makes obtaining converged solutions to it difficult in practical flow problems. Nevertheless, this approach motivates the use of an algebraic expression for the Reynolds stress anisotropy as a function of turbulent kinetic energy, dissipation rate, and mean velocity gradients — an approach that is used in the development of another group of turbulence models: non-linear eddy-viscosity models. Non-linear eddy-viscosity models retain the simplicity of linear eddy-viscosity models whilst providing the means for modelling the anisotropy of the Reynolds stresses. Extending the tensorial stress-strain relation of the Reynolds stresses to a more appropriate non-linear form has been proven to improve the predictions in complex

flows, as has been reviewed in [26–30]. One of the earliest non-linear eddy-viscosity formulations, the quadratic $k-\varepsilon$ model by Nisizima and Yoshizawa [31], demonstrates the effectiveness of the non-linear Reynolds stress formulation in producing the correct anisotropic turbulence intensities in a turbulent channel flow and a Couette-Poiseuille flow. Speziale [32] also proposes a quadratic $k-\varepsilon$ model which shows improved separation and reattachment predictions in a backward-facing step problem. The cubic $k-\varepsilon$ model of Craft et al. [12] gives a more accurate prediction of the asymmetric velocity profile resulting from streamline curvature effects when tested on a curved channel flow compared to the linear version. The later version of the model [33], which includes an added transport equation for a stress anisotropy invariant, shows more realistic normal stress levels near the stagnation point of an impinging jet, whereas linear models are known to give erroneous predictions. Suga and Abe [34] add a transport equation for the invariants of the stress anisotropy tensor in their cubic $k-\varepsilon$ model and show encouraging performance in capturing anisotropic turbulence and thermal fields near both wall and shear-free boundaries. A cubic $k-\varepsilon$ model by Apsley and Leschziner [35] gives a more accurate prediction of cross-channel asymmetry of the velocity and turbulent stress profiles on a plane asymmetric diffuser compared to the linear $k-\varepsilon$ model.

In contrast with the Explicit Algebraic Reynolds Stress Models (EARSM), e.g. [36–38], which are derived from solving an equilibrium approximation to a Reynolds stress transport model, most non-linear eddy-viscosity models use a constitutive relation for the Reynolds stress tensor obtained from a generic, expanded expression for the anisotropy, derived first by Pope [17] using a tensor invariant theory, and their coefficients are functions of the invariants. This approach is also adopted in this work. However, the specific dissipation (or turbulence frequency), ω, is used as the turbulence scale since it has been shown to perform better for modelling boundary layers and flows under adverse pressure gradients [39, 40]. To the authors' knowledge, with the exception of the works of Larsson [41], Song et al. [42], and Abe et al. [43], non-linear eddy-viscosity models have not been based on the specific dissipation rate, ω, but instead are based on the dissipation rate, ε (although the non-linear $k-\omega$ model by Larsson [41] is a modified version of the non-linear $k-\varepsilon$ model of Shih et al. [44] for use in a $k-\omega$ framework). The cubic $k-\omega$ model by Song et al. [42] shows an improvement over the linear $k-\omega$ model but returns an underprediction of the anisotropy level of the Reynolds stresses in the near-wall region and it is highlighted that a near-wall modification is needed. The quadratic $k-\omega$ model of Abe et al. [43] includes a modification for strong Reynolds stress anisotropy in the near-wall region; however, the model uses additional strain and rotation terms for the wall modification and includes wall-normal distance in its formulation, which is generally known to show limitations in applications involving complex geometries.

In this work, a new non-linear turbulence model is developed based on the classic $k-\omega$ model [45]. Since this is the simplest version of an ω-based model, applying it as the base model allows a direct observation of the effectiveness of the proposed modelling approach. A simple scaling term to provide a consistent formulation of the non-linear model is proposed. The resulting model is extended to incorporate an enhanced treatment of near-wall turbulence anisotropy. The modification proposed relies only on local variables to ensure its robustness for complex configurations. The performance of the proposed model is demonstrated by testing it on a number of simple and complex 2-D and 3-D flow configurations. A number of canonical cases involving simple shear, boundary layers, and curvature features are presented, followed by more complex cases which involve separation and swirling to

show the applicability of the new model to more complex geometries.

2. New model development

This section describes the philosophy and development of the proposed model. The non-linear stress-strain relation for the Reynolds stress tensor used in the model is presented first. The formulation of the proposed model is then discussed followed by its initial calibration. Finally, a modification for modelling the near-wall anisotropy is presented.

2.1. The closure problem and the non-linear stress-strain relationship

RANS equations for the three-dimensional flow of an incompressible, viscous, and isothermal fluid are:

$$\frac{\partial U_j}{\partial x_j} = 0 \tag{1}$$

$$\frac{\partial U_i}{\partial t} + U_j \frac{\partial U_i}{\partial x_j} = -\frac{1}{\rho}\frac{\partial P}{\partial x_j} + \frac{\partial}{\partial x_j}\left(\nu \frac{\partial U_i}{\partial x_j} - \overline{u_i' u_j'}\right) \tag{2}$$

Here x_j are the spatial Cartesian co-ordinates. U and P are the mean velocity and pressure, respectively. The term $\overline{u_i' u_j'}$ is the Reynolds stress tensor that arises from Reynolds-averaging the Navier-Stokes equations. It introduces additional unknown quantities resulting in the so-called 'closure' problem since there are more unknowns than equations available to solve the system. RANS turbulence models incorporate the effects that turbulence has on the mean flow via $\overline{u_i' u_j'}$, whilst simultaneously providing 'closure' to the system of equations. In this work, 'closure' is achieved using a non-linear stress-strain approach based on an anisotropy tensor formulation.

Linear eddy-viscosity models assume that $\overline{u_i' u_j'}$ is proportional to the local mean rate of strain (S_{ij}). Implicitly, they also assume that turbulence is isotropic i.e. the mean velocity fluctuations components are equal ($\overline{u'} = \overline{v'} = \overline{w'}$). The departure of the Reynolds stress tensor from isotropy is defined by the Reynolds stress anisotropy tensor, a_{ij}, described in its non-dimensional form as:

$$a_{ij} = \frac{\overline{u_i' u_j'}}{k} - \frac{2}{3}\delta_{ij} \tag{3}$$

where k is the turbulent kinetic energy and is defined as $k = (\overline{u_i' u_i'})/2$. The anisotropy tensor formulation above can be used to develop non-linear eddy-viscosity models. It extends in a rigorous manner the one-term tensor representation used for linear eddy-viscosity models into a more generalised form. Using the formulation first suggested by Pope [17], a_{ij} can be formally expressed as a function of mean velocity-gradient tensor (separated into mean strain

and vorticity rate, S_{ij} and Ω_{ij}, respectively) and turbulent quantities, e.g. using the turbulent kinetic energy (k) and the specific dissipation rate (ω):

$$a_{ij} = f(k, \omega, S_{ij}, \Omega_{ij}) \tag{4}$$

Based on the principle of reducibility of higher order tensors according to the Cayley-Hamilton theorem, the anisotropy tensor can be expressed as a polynomial. Using the invariant theory in [46, 47], higher order tensor terms for a symmetric traceless second-order tensor, such as a_{ij}, can be described as a finite tensor polynomial containing ten independent terms:

$$a_{ij} = \sum_{n=1}^{10} \beta_{n-1} T_{ij}^{(n)} \tag{5}$$

where β_{n-1} are the anisotropy expansion terms and $T_{ij}^{(n)}$ are tensor bases formed from S_{ij} and Ω_{ij}. The reader is referred to [17, 27] for more details on the derivation of the tensor bases. They are:

$$\begin{aligned}
T_{ij}^{(1)} &= S_{ij} \\
T_{ij}^{(2)} &= S_{ik}S_{kj} - II_S\delta_{ij}/3 \\
T_{ij}^{(3)} &= S_{ik}\Omega_{kj} - \Omega_{ik}S_{kj} \\
T_{ij}^{(4)} &= \Omega_{ik}\Omega_{kj} - II_\Omega\delta_{ij}/3 \\
T_{ij}^{(5)} &= S_{ik}S_{kl}\Omega_{lj} - \Omega_{ik}S_{kl}S_{lj} \\
T_{ij}^{(6)} &= S_{ik}\Omega_{kl}\Omega_{lj} + \Omega_{ik}\Omega_{kl}S_{lj} - 2IV\delta_{ij}/3 \\
T_{ij}^{(7)} &= S_{ik}S_{kl}\Omega_{lp}\Omega_{pj} + \Omega_{ik}\Omega_{kl}S_{lp}S_{pj} - 2V\delta_{ij}/3 \\
T_{ij}^{(8)} &= S_{ik}\Omega_{kl}S_{lp}S_{pj} - S_{ik}S_{kl}\Omega_{lp}S_{pj} \\
T_{ij}^{(9)} &= \Omega_{ik}S_{kl}\Omega_{lp}\Omega_{pj} - \Omega_{ik}\Omega_{kl}S_{lp}\Omega_{pj} \\
T_{ij}^{(10)} &= \Omega_{ik}S_{kl}S_{lp}\Omega_{pq}\Omega_{qj} - \Omega_{ik}\Omega_{kl}S_{lp}S_{pq}\Omega_{qj}
\end{aligned} \tag{6}$$

The independent scalar invariants are defined as:

$$\begin{aligned}
II_S &= S_{kl}S_{lk} \\
II_\Omega &= \Omega_{kl}\Omega_{lk} \\
III_S &= S_{kl}S_{lm}S_{mk} \\
IV &= S_{kl}\Omega_{lm}\Omega_{mk} \\
V &= S_{kl}S_{lm}\Omega_{mn}\Omega_{nk}
\end{aligned} \tag{7}$$

The first term in the anisotropy tensor formulation ($T_{ij}^{(1)} = S_{ij}$) can be shown to be the only term retained in linear eddy-viscosity models, which use the Boussinesq hypothesis to model the Reynolds stress tensor, $\overline{u_i' u_j'}$, resulting in:

$$\overline{u_i' u_j'} = -2\nu_T S_{ij} + \frac{2}{3} k \delta_{ij} \tag{8}$$

where ν_t is the turbulent eddy viscosity and its definition depends on the choice of turbulence model. For example, using the $k-\omega$ model, this is defined as $\nu_t = k/\omega$.

For implementation purposes, the Reynolds stress tensor for a non-linear formulation can be expressed using the standard definition of the Boussinesq hypothesis, as shown in Eq. (8), with an added tensor, $\widetilde{a_{ij}}$, to incorporate the non-linear terms from Eq. (5), such that:

$$\widetilde{\overline{u_i' u_j'}} = \overline{u_i' u_j'} + \widetilde{a}_{ij} k \tag{9}$$

The extra anisotropy tensor term above, $\widetilde{a}_{ij}$, is simply the general form presented in (5) without the first tensor base ($T_{ij}^{(1)}$), that is:

$$\widetilde{a}_{ij} = \sum_{n=2}^{10} \beta_{n-1} T_{ij}^{(n)} \tag{10}$$

The separation of the isotropic and anisotropic parts of the Reynolds stress tensor allows a relatively straightforward incorporation of the extra anisotropy tensor, $\widetilde{a}_{ij}$, into an existing linear eddy-viscosity model implementation. In the context of non-linear eddy-viscosity modelling the extra anisotropy expansion terms, β_{n-1}, are determined using using physical constraints combined with experimental and numerical data, e.g. [12, 26, 31, 32, 48].

2.2. Proposed model formulation

The new non-linear turbulence model is based on the original $k-\omega$ model [45]. The model solves for the turbulent kinetic energy, k, and specific turbulence dissipation rate, ω, using the following transport equations:

$$\frac{Dk}{Dt} = \widehat{P_k} - \beta^* k\omega + \frac{\partial}{\partial x_j}\left[\left(\nu + \sigma_k \frac{k}{\omega}\right)\frac{\partial k}{\partial x_j}\right] \tag{11}$$

$$\frac{D\omega}{Dt} = C_{\omega,1} P_k \frac{\omega}{k} - C_{\omega,2}\omega^2 + \frac{\partial}{\partial x_j}\left[\left(\nu + \sigma_\omega \frac{k}{\omega}\right)\frac{\partial \omega}{\partial x_j}\right] \tag{12}$$

$$\nu_T = \frac{k}{\omega} \tag{13}$$

The closure constants preserve the same values as the original $k-\omega$ model i.e. $\beta^* = 0.09$, $C_{\omega,1} = 0.52$, $C_{\omega,2} = 0.072$, $\sigma_k = 0.5$, and $\sigma_\omega = 0.5$. The production of turbulent kinetic energy used in the ω equation is modelled using the classical stress-strain approach:

$$P_k = -\overline{u_i' u_j'} \frac{\partial U_i}{\partial x_j} \tag{14}$$

where $\overline{u_i' u_j'}$ is estimated using the Boussinesq hypothesis as shown in Eq. (8). A production limiter [49] is used in the k equation to prevent excessive production in regions where ω has low values, such as in the freestream or near the edge of boundary layers. This limiter has also been found to be useful for eliminating unphysical buildup of eddy viscosity in stagnation regions [50]. The limiter is defined as:

$$\widehat{P_k} = \min(\widetilde{P_k}, 20\beta^*\omega k) \tag{15}$$

The production of turbulent kinetic energy is modelled using the classical stress-strain approach. However, the Reynolds stress tensor is approximated using Eq. (9) through which the non-linear formulation is introduced. Therefore:

$$\begin{aligned} \widetilde{P_k} &= -\widetilde{\overline{u_i' u_j'}} \frac{\partial U_i}{\partial x_j} \\ &= -\left(\overline{u_i' u_j'} + \widetilde{a}_{ij} k\right) \frac{\partial U_i}{\partial x_j} \end{aligned} \tag{16}$$

Although the use of Eq. (14) and Eq. (16) for the production of ω in Eq. (12) has been found to produce similar results, the use of Eq. (14) is found to show improved numerical behaviour and convergence. Eq. (16) is used in the production of k in Eq. (11) to introduce the non-linear Reynolds stress anisotropy tensor.

The extra anisotropy tensor, $\widetilde{a}_{ij}$, defined in Eq. (10), is a tensor polynomial. For the new model, a quadratic formulation is proposed. Therefore, $\widetilde{a}_{ij}$ reduces to the following formulation which retains up to $n = 4$ in the polynomial:

$$\widetilde{a}_{ij} = C_\mu \left[\beta_1 \left(S_{ik} S_{kj} - \frac{1}{3} II_S \delta_{ij} \right) + \beta_2 \left(S_{ik}\Omega_{kj} - \Omega_{ik} S_{kj} \right) + \beta_3 \left(\Omega_{ik}\Omega_{kj} - \frac{1}{3} II_\Omega \delta_{ij} \right) \right] \tag{17}$$

Since $\widetilde{a}_{ij}$ takes into account the mean strain and vorticity rates at a quadratic level, it can cause the production of turbulent kinetic energy to decrease significantly, especially at the start of a calculation. This can result in k becoming negative, hence non-physical. Therefore, a realisability condition is applied. The realisability formulation used for the present model is similar to that proposed by Kimura et al. [51], which ensures non-negativity of the normal Reynolds stresses and the Schwarz' inequality for the Reynolds shear stresses. It is based on the realisability condition proposed by Shih et al. [52] which employs time scale ratios based on the mean strain and vorticity rates. The realisability constraint is included in the new model using:

$$C_\mu = \frac{1}{1 + 0.1M^2} \tag{18}$$

M is a parameter that takes the maximum between the strain and rotation rates in the form of their dimensionless invariants, $\tilde{S}$ and $\tilde{\Omega}$, respectively:

$$M = \max(\tilde{S}, \tilde{\Omega}) \quad , \quad \tilde{S} = \frac{1}{\omega}\sqrt{2S_{ij}S_{ij}} \quad , \quad \tilde{\Omega} = \frac{1}{\omega}\sqrt{2\Omega_{ij}\Omega_{ij}} \tag{19}$$

It is important to note that the expansion terms β_1, β_2, and β_3 (or β_n for convenience) in Eq. (17) are not constants. In addition to satisfying dimensional analysis, β_n must relate to turbulent scales in a consistent manner. A number of formulations have been used in literature. More complex approaches include the non-linear models of Abe et al. [53] and Hellsten [54] in which the expansion terms are derived based on the EARSM concept [36, 38, 55]. A simpler approach uses a formulation related only to the turbulent scales, e.g. k^2/ε^2 multiplied by a dimensionless scalar [12, 26, 31, 56]. A similar approach is proposed here, however, using a scaling term proportional to $1/\omega^2$ to provide dimensional consistency. This is also consistent with flow behaviour near solid boundaries since it allows the anisotropy tensor to become negligible at the wall where turbulence length scales become smaller as the wall is approached until isotropy is reached at the smallest scales. The proposed functional form for β_n is:

$$\beta_n = \frac{C_{\beta,n}}{\max(\omega, \kappa S)^2} \tag{20}$$

where S is the magnitude of the mean strain rate. The limiter in the denominator is introduced to ensure stability by reducing the influence of the non-linear formulation in regions where the mean strain and vorticity rates are high, in particular, stagnation regions and developing boundary layers. The constant κ is set to 2.5. This resulted in stable solutions whilst ensuring that the anisotropy formulation remained active in the freestream and developed boundary layers. Finally, $C_{\beta,n}$ are the expansion coefficients which require calibration.

2.3. Boundary conditions

At wall boundaries, no-slip conditions apply which sets the velocity components and the turbulent kinetic energy to be equal to zero. The specific dissipation rate, ω, is resolved using the classic solution for smooth walls:

$$\omega_{wall} = \frac{6\nu}{C_{\omega,2}y^2} \tag{21}$$

2.4. Baseline model: calibration and initial assessment

In order to complete the model formulation, three coefficients need to be calibrated: $C_{\beta,1}$, $C_{\beta,2}$, and $C_{\beta,3}$. The coefficient $C_{\beta,3}$ originates from the third term on the right-hand side of Eq. (17) (which contains the expansion term β_3). This term, however, has been found to cause unphysical behaviour in rotating isotropic flow [57], as well as, to cause a model to violate realisability [14]. Therefore, $C_{\beta,3}$ is taken as 0.

In the baseline non-linear $k-\omega$ model, $C_{\beta,1}$ and $C_{\beta,2}$ are considered to be constants. They were calibrated for parallel channel flow at various Reynolds numbers using DNS results

from [58]. The calibrated model was subsequently tested on a flat plate to ensure that the predictions agreed with the theoretical turbulent skin friction distribution. The calibrated values are presented in Table 1.

Table 1: Summary of coefficients for the baseline non-linear $k-\omega$ model

$C_{\beta,1}$	$C_{\beta,2}$
10.2	8.0

In a simple channel flow case, it can be observed, from Figure 1, that the baseline non-linear $k-\omega$ model offers improved predictions of the Reynolds stresses compared to the standard $k-\omega$ model. The spanwise velocity fluctuations, $\overline{w'w'}$, are predicted by the baseline model at values closely matching the DNS data. There is also an improvement in the prediction of streamwise velocity fluctuations, $\overline{u'u'}$, and a decrease in wall-normal fluctuations, $\overline{v'v'}$. However, closer to the wall ($y/h < 0.2$) the anisotropy level is under predicted. The approach to calibrate $C_{\beta,n}$ as constants is one that many existing non-linear models have proposed, e.g. [31, 32, 48, 59]. Its inclusion in the present work allows a direct assessment of the effectiveness of extending the non-linear $k-\omega$ model to account for strong anisotropy near solid boundaries. This extension will be discussed in the next section.

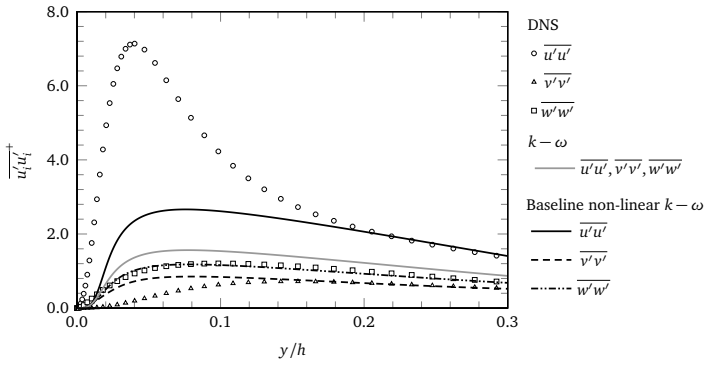

Figure 1: Reynolds stresses in a plane channel flow at $Re_\tau = 180$. Markers correspond to DNS data [58].

2.5. Modification for strong near-wall anisotropy

Abe et al. [43] proposed a formulation to model near-wall anisotropy using tensorial terms, in addition to strain and rotation rates, which depend on wall-direction indicators. This approach is not pursued in the present model since it increases complexity and computational time. Instead, strong near-wall anisotropy is incorporated into the model using functional forms of the expansion coefficients $C_{\beta,1}$ and $C_{\beta,2}$ that depend only on the modelled turbulent scales, k and ω.

The turbulent boundary layer can be broadly divided into 3 distinct regions: the viscous sublayer, the buffer layer, and the log layer. Within the viscous sublayer, the flow can be considered to be laminar and velocity fluctuations vanish at the wall due to the no-slip condition. Therefore, the expansion coefficients, $C_{\beta,n}$, need to account for viscous damping towards the wall. Moving away from the wall, as the buffer layer is approached and due to

strong non-equilibrium, turbulent perturbations penetrate the viscous sublayer. This results in a significant transport of Reynolds stresses towards the wall. Thus, $C_{\beta,n}$ should account for an increase in turbulence production here. Finally, entering the log layer, anisotropy levels decrease as observed in DNS [58]. Therefore, the expansion coefficients should decrease through the buffer layer towards a constant value in the log layer. In the log layer, $C_{\beta,n}$ should return to the calibrated values used in the baseline non-linear $k-\omega$ (Table 1). To incorporate these effects, the expansion coefficients, $C_{\beta,n}$, are modelled as:

$$C_{\beta,n} = f_{V,n} + f_{B,n} + f_{L,n} \tag{22}$$

The functions $f_{V,n}$, $f_{B,n}$, and $f_{L,n}$ control the value of the expansion coefficients within the viscous, buffer, and log regions, respectively. They are defined as:

$$\begin{aligned} f_{V,n} &= C_{V,n} f_1 f_2 \\ f_{B,n} &= C_{B,n} f_1 f_3 \\ f_{L,n} &= C_{L,n}(1-f_3) \end{aligned} \tag{23}$$

where

$$f_1 = 1 - exp\left(\frac{-Re_T^{C_1}}{C_2}\right) \quad , \quad f_2 = exp\left(\frac{-Re_T^{C_3}}{C_4}\right) \quad , \quad f_3 = 1 - tanh\left(\frac{Re_T^{C_5}}{C_6}\right) \tag{24}$$

The damping functions f_1, f_2, and f_3 have been formulated such that they are only functions of the turbulence Reynolds number, $Re_T = k/\nu\omega$. The coefficients $C_{V,n}$, $C_{B,n}$, $C_{L,n}$, and C_1 to C_6 need to be calibrated.

2.6. Near-wall modified model: calibration and initial assessment

For the calibration of the coefficients that originate from the near-wall modification proposed above, it is assumed that the expansion coefficients, $C_{\beta,n}$, can be treated as 'universal' i.e. they are not dependent, or are only weakly dependent, on the Reynolds number of the flow. Furthermore, it is assumed that any effects due to turbulence are also independent of $C_{\beta,n}$ since the non-linear term, $\widetilde{a_{ij}}k$, that is included in the non-linear formulation of the Reynolds stress tensor in Eq. (9), is proportional to the turbulent eddy viscosity, ν_T. The validity of these assumptions will be explored in this section. The calibration method is briefly presented first.

The near-wall model was calibrated for plane channel flow using DNS data [58] at a Reynolds number of 180 (based on half-width of the channel and the wall shear velocity). This simple flow can be described by the only non-zero velocity gradient: $\lambda = dU/dy$. An analytical solution can be found for the non-linear Reynolds stress tensor (i.e. $\widetilde{\overline{u_i'u_j'}} = \overline{u_i'u_j'} + \widetilde{a}_{ij}k$). Therefore, for fully developed flow, it can be shown that the proposed non-linear model predicts the normal stresses as:

$$\overline{u'u'} \approx \frac{1}{\omega^2}\lambda^2 k\left(\frac{1}{12}C_{\beta,1}+\frac{1}{2}C_{\beta,2}\right)+\frac{2}{3}k$$
$$\overline{v'v'} \approx \frac{1}{\omega^2}\lambda^2 k\left(\frac{1}{12}C_{\beta,1}-\frac{1}{2}C_{\beta,2}\right)+\frac{2}{3}k$$
$$\overline{w'w'} \approx \frac{1}{\omega^2}\lambda^2 k\left(-\frac{1}{6}C_{\beta,1}\right)+\frac{2}{3}k \tag{25}$$

An optimisation algorithm was used to determine the distributions of the expansion coefficients, $C_{\beta,n}$, that minimise the least-squares error of the model predictions obtained with the equations above compared with the DNS benchmark results. The result is presented in Figure 2. The profiles for $C_{\beta,1}$ and $C_{\beta,2}$ are similar and therefore for clarity, only the $C_{\beta,1}$ profile is shown here. The velocity profile in wall coordinates as well as the law of the wall profile are also shown for reference.

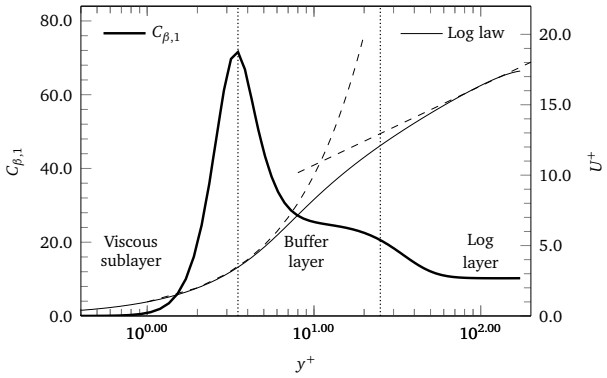

Figure 2: Profile of the expansion coefficient calculated using the near-wall modification in reference to the law of the wall.

The final step in the calibration procedure is to find the coefficients, $C_1, C_2 \ldots C_6$, of the damping functions defined in Eq. (24). They were estimated using curve fitting based on the default Trust-Region Dogleg Method implemented in Matlab. The recommended coefficients for the non-linear $k-\omega$ model with enhanced near-wall anisotropy are summarised in Table 2. Notice that the value of the coefficients in the log region, i.e. $C_{L,1}$ and $C_{L,2}$, are equal to the constant values adopted in the baseline non-linear $k-\omega$ model for the expansion coefficients, $C_{\beta,1}$ and $C_{\beta,2}$, shown in Table 1.

Table 2: Coefficients for the present model

C_1	C_2	C_3	C_4	C_5	C_6
0.92	0.01	0.40	0.18	1.90	70.00

$C_{V,1}$	$C_{B,1}$	$C_{L,1}$	$C_{V,2}$	$C_{B,2}$	$C_{L,2}$
160.0	25.0	10.2	122.0	15.0	8.0

The Reynolds stresses predicted using this extension of the proposed model for plane channel flow are presented in Figure 3, plotted against the wall-normal distance. It can be observed that, for $y/h < 0.2$, the prediction of wall-normal fluctuations near the wall is significantly improved compared to the baseline non-linear $k-\omega$ model. The predicted peak level of $\overline{u'u'}$ is improved by approximately 30%. Overall, all three components are underpredicted compared to the DNS data. This is due to the inherent underprediction of turbulent kinetic energy, k, made by the underlying $k-\omega$ model (upon which the present model is based).

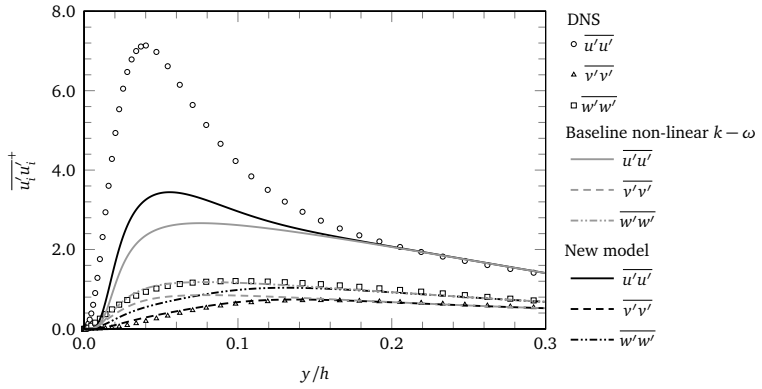

Figure 3: Reynolds stresses in a plane channel flow at $Re_\tau = 180$. Markers correspond to DNS data [58].

Anisotropy profiles, a_{ij}, resulting from the proposed near-wall modification are presented in Figure 4 alongside the predictions from the baseline $k-\omega$ model. The new model is shown to perform well in predicting the near-wall anisotropy levels. This shows that the combination of the quadratic Reynolds stress tensor formulation and the proposed near-wall modifications result in a marked improvement in the prediction of anisotropy. In particular, improvements in the peak values of approximately 100% can be observed compared to the baseline model.

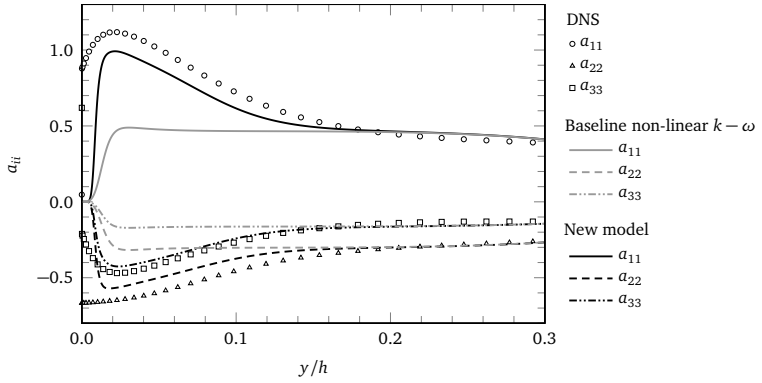

Figure 4: Reynolds stress anisotropy in a plane channel flow at $Re_\tau = 180$. Markers correspond to DNS data [58].

To ensure that the 'universality' assumption made when calibrating the near-wall modi-

fication is valid, the model has been tested at different Reynolds numbers. The results are presented in Figure 5. Again, the model shows improved predictions in the distribution of the anisotropy level within the near-wall region, particularly for $y/h < 0.05$ compared to the DNS data for both cases.

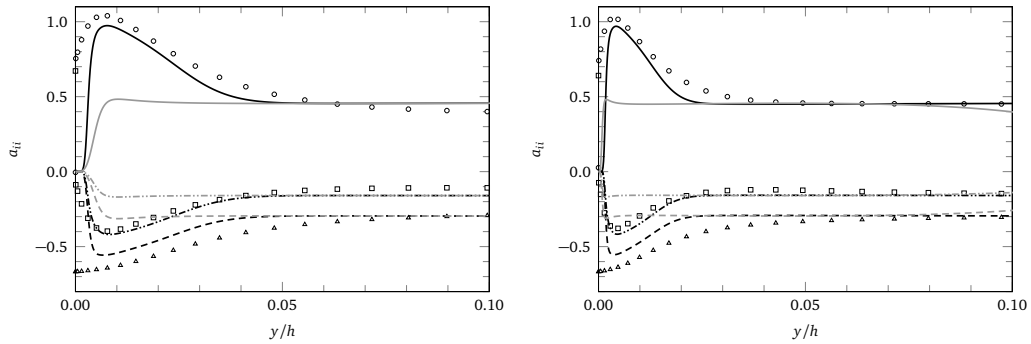

(a) $Re_\tau = 550$ (b) $Re_\tau = 1000$

Figure 5: Reynolds stress anisotropy in a plane channel flow at $Re_\tau = 550$ and $Re_\tau = 1000$. Markers correspond to DNS data [58]. Line notations are the same as Figure 4.

3. Test cases

The initial performance of the proposed non-linear $k-\omega$ model (with the near-wall modification) has been established in the previous section using a simple shear flow. It is now validated and tested further by applying it to a range of cases with different flow features. The configurations tested in this section include: (i) a flat plate at zero-pressure-gradient, (ii) a U-bend channel, (iii) a planar diffuser with a downstream monolith, and (iv) a swirling flow in sudden expansion diffuser with a downstream monolith. The last two configurations are particularly challenging and relevant to automotive exhaust systems.

The predictions of the proposed model are assessed in comparison against the predictions of the standard $k-\omega$ model. To compare the performance of the new model with existing non-linear eddy-viscosity models, two other non-linear (NL) models are also included. These are: the high-Re realisable quadratic $k-\varepsilon$ model of Shih et al. [52] and the low-Re cubic $k-\varepsilon$ model of Lien et al. [60].

3.1. Numerical method

Due to the relative ease of implementing new turbulence models, the model equations are implemented in and tested using the open-source CFD package OpenFOAM 6 [61]. It has been gaining popularity in academia and industry, and its validity for scientific research has been established [62, 63]. The implementation of the model follows the methodology suggested in [64]. A steady state incompressible flow solver `simpleFoam` (consistent), based on the SIMPLEC algorithm, available in OpenFOAM is used to perform the calculations. The various terms in the model equations are discretised using the standard finite volume discretisation of Gaussian integration. The gradient terms are computed using linear interpolation. For Laplacian terms, diffusion coefficients are discretised using linear interpolation. Finally,

divergence terms are evaluated using a blended linear upwind scheme offering first/second order accuracy. This scheme is selected because it provides a suitable compromise between stability and accuracy. The simulations were considered converged if the normalised residuals dropped below 10^{-5}, with the exception of the cases involving a porous region (convergence was monitored based on the pressure drop and a flattening of the residuals). For these simulations, the gradient terms for the turbulence quantities (k and ω) were limited using a cell-based limiter. This is common practice in commercial packages to improve solution stability for complex configurations by ensuring that the face values that are interpolated from cell values are bounded by the values of the neighbouring cells [65, 66].

3.2. Zero-Pressure-Gradient flat plate

This is a classical test case for testing the performance of a turbulence model in predicting boundary layer flow and is also useful for testing the correct implementation of a model. The simulation is set up to match the T3B case by ERCOFTAC [67] which is a zero-pressure-gradient flat plate at freestream turbulence intensity of $Tu_\infty = 6.0\%$. A schematic of the domain is shown in Figure 6. At the inlet, the freestream velocity is $U_\infty = 9.4\ m/s$ and the turbulent kinetic energy is calculated based on the turbulence intensity. The specific dissipation rate, ω, and dissipation rate, ε, are estimated using eddy viscosity ratio of $\nu_R = \nu_t/\nu = 100$. A slip condition was used on the top boundary. A velocity inlet and a pressure outlet are prescribed. At the wall, the turbulent kinetic energy, specific dissipation rate, and velocities are set up as detailed in Section 2.3 for the proposed model and the $k-\omega$ model and as prescribed in the original works for the other non-linear models [52, 60] (since this is true for all the simulations presented here, it will not be restated). Grid independence is achieved by ensuring that the change in the mean velocities across a number of axial stations and the change in the average skin friction coefficient across the plate is sufficiently low (less than 0.5%). This results in a grid of $635 \times 140 \times 1$ cells, giving a total of 88,900 cells, for the low-Re models (the new model, the standard $k-\omega$ model, and the Lien cubic $k-\varepsilon$ model). The corresponding maximum y^+ value was 0.61. For the high-Re model (the Shih quadratic $k-\varepsilon$ model), the grid has $635 \times 42 \times 1$ cells, giving a total of 26,600 cells. The corresponding maximum y^+ value was 35.

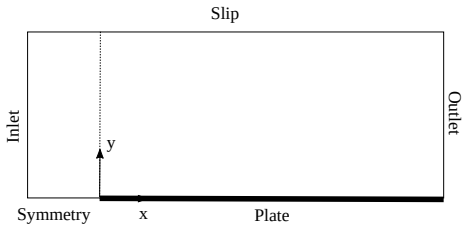

Figure 6: Computational domain of the T3 flat plate case

Figure 7 presents the skin friction coefficient distribution along the plate predicted using the tested models. The results from the new model and the $k-\omega$ model are identical and closely match the experimental values for $Re_x > 0.5 \times 10^6$. This result demonstrates that the formulation of the new model retains the ability of the underlying $k-\omega$ model to correctly

predict the skin friction of a turbulent boundary layer. It also provides confidence that the model has been implemented correctly. The Shih NL $k-\varepsilon$ and Lien NL $k-\varepsilon$ models show lower skin friction coefficient predictions compared to the theoretical turbulent line for $Re_x < 0.3\times10^6$, and closely match the turbulent line and the experimental values downstream. This behaviour has been observed previously on fully-turbulent $k-\varepsilon$ models [68, 69].

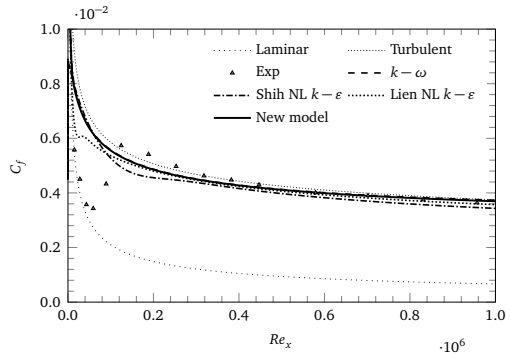

Figure 7: Streamwise skin friction distribution on the T3B case. Markers correspond to ERCOFTAC experimental data [67].

Profiles of the Reynolds stress components are shown in Figure 8, normalised with the freestream velocity. Reynolds stress predictions are observed at two stations on the plate at which the Reynolds numbers based on the streamwise distance are $Re_x = 183,000$ and $556,000$. These correspond to locations where the flow is found to be fully turbulent in the experiments, which are suitable for the validation of the proposed model (since it is a fully-turbulent model). The three tested non-linear models correctly predict the experimental trend of the anisotropic Reynolds stress profiles at both locations. Although the Shih NL $k-\varepsilon$ model correctly shows the rise in streamwise fluctuations and decrease in the other two components of the Reynolds stresses, it can be observed to suffer from its high-Re formulation, and consequently the high y^+ grid that it requires. The Lien NL $k-\varepsilon$ model returns an underprediction of the Reynolds stress anisotropy level, highlighted by the underprediction of the streamwise fluctuations and the close predictions for the other two components at both locations. The new model shows predictions of the Reynolds stresses closer to the experimental data at $Re_x = 183,000$ compared to the other tested models, although it underpredicts the streamwise fluctuations closer to the wall. This can be attributed to the rise of turbulent kinetic energy, and specifically streamwise fluctuation, during transition. Further along the plate at $Re_x = 556,000$, away from the transition region, the new model predictions are closer to the experimental values overall on all three components. Such an agreement is remarkable, especially considering the relative simplicity of the proposed near-wall modification and the fact that it has been calibrated based on a single case.

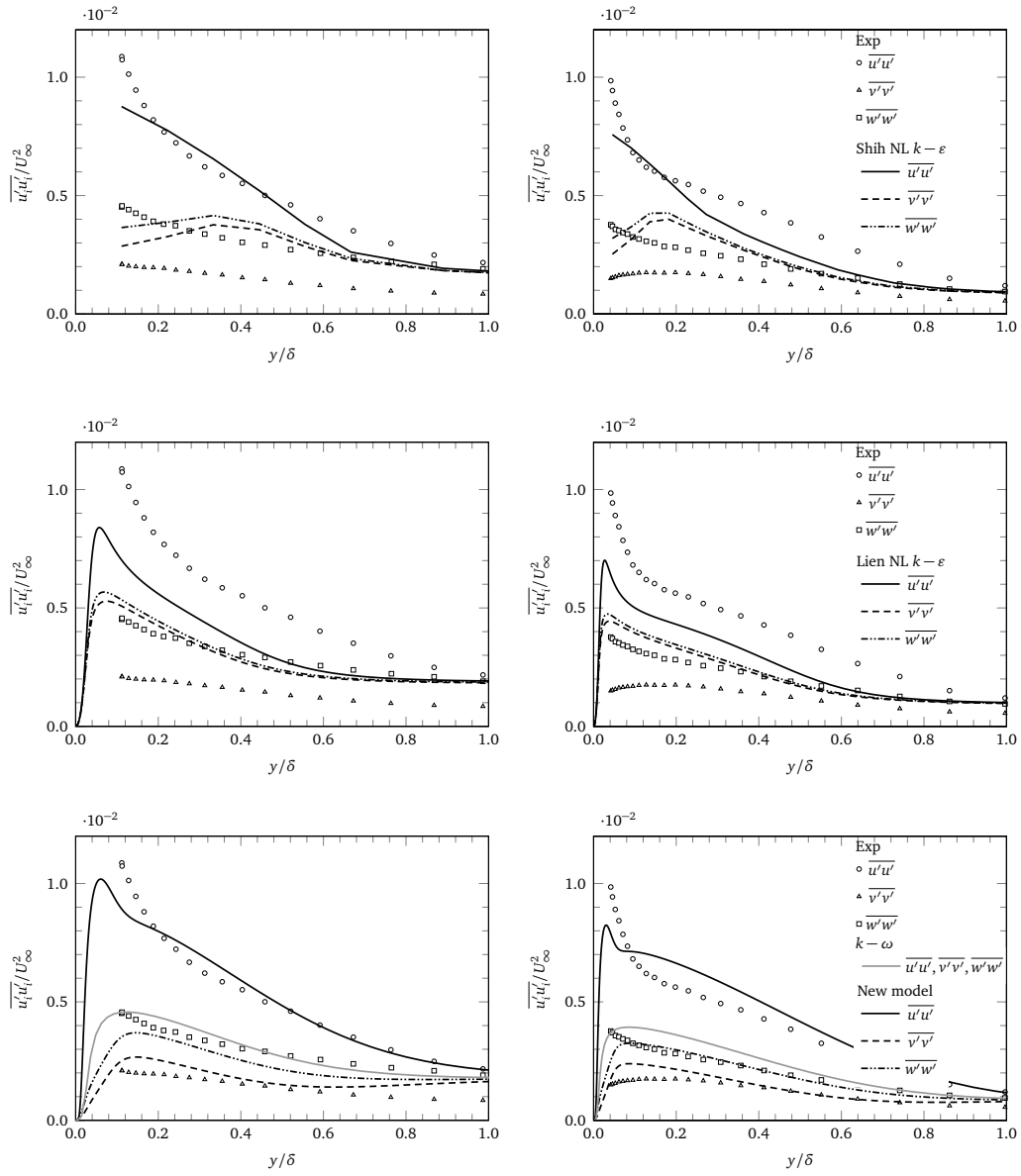

Figure 8: Velocity fluctuations at local Reynolds numbers $Re_x = 183,000$ (left) and $Re_x = 556,000$ (right) on the T3B case. Markers correspond to experimental data [67].

3.3. Curved channel

The U-bend curved channel configuration is widely used for validating turbulence models against the effects of curvature, as well as internal shear layers. The case tested here reproduces the experiment by Monson et al. [70]. A schematic of the domain used for the simulation is shown in Figure 9. The Reynolds number is 10^6 based on the inlet velocity and

the height of the channel, h. The flow is simulated using a two-dimensional domain since the aspect ratio of the rectangular channel in the experiment is 10 and the flowfield is found to be reasonably two-dimensional throughout. A precursor computation is carried out to match the boundary layer thickness recorded in the experiment, that is, $0.25h$ at the inlet. The inlet is located at $x/h = -4$ from the start of the bend and the outlet is placed at a distance of $6h$ from the end of the bend. The turbulence intensity at the inlet of the channel reported in the experiment is 1.16%. The turbulent kinetic energy is calculated from the freestream turbulence intensity, and the eddy viscosity ratio is set to 38.7. Grid independence is achieved by ensuring that the changes in the mean velocities across a number of locations along the channel as well as the pressure drop across the domain are sufficiently low (around 2.5% here). This results in a hybrid grid consisting of 85,000 cells for the low-Re models with a prism layer of 60 cells for capturing the boundary layer. The corresponding maximum y^+ value was 0.69. For the high-Re model, a hybrid grid of 43,000 cells was used with a prism layer of 20 cells. The corresponding maximum y^+ value was 34.

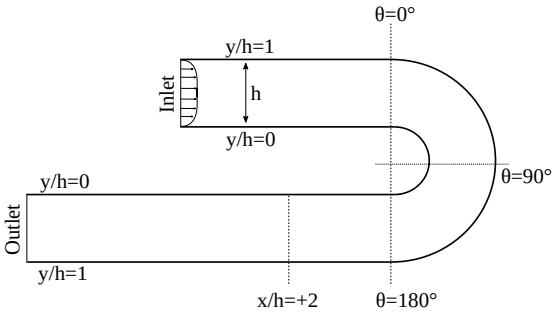

Figure 9: Computational domain of the curved channel flow case

Non-dimensional velocity profiles are presented in Figure 10. They are plotted against the wall-normal distance from the inner wall of the channel, y, and are non-dimensionalised with h. The exit of the bend is located at $\theta = 180\,\text{deg}$ and $x/h = +2$ denotes a location $2h$ downstream of the bend (see also Figure 9).

As the flow goes into the bend, the flow accelerates at the inner wall and decelerates at the outer wall. In the last half of the bend flow separation is known to occur at the inner wall due to a severe adverse pressure gradient [71]. In Figure 10, at $\theta = 180\,\text{deg}$, the experimental results show the presence of reversed flow near the inner wall at the exit of the bend. The velocity profiles predicted by all the tested models show that separation at the inner wall is captured. However, the level of flow separation is generally underpredicted, with the new model showing some improvement compared to the other models. Across the rest of the channel, the velocity profile is almost flat, except near the concave wall where the boundary layer is thin as a result of the destabilising curvature [72]. Downstream of the bend, at $x/h = +2$, the flow reattaches at the inner wall and accelerates at the outer wall. The new model predicts a slower recovery than the $k-\omega$ model at the inner wall, comparable to the other non-linear models. However, it predicts the acceleration at the outer wall more accurately, as shown in Figure 10 (b).

Figure 11 (a) shows that at the exit of the bend all the tested models fail to capture the characteristic turbulent kinetic energy profiles for $0.2 < y/h < 0.9$, possibly as a result of underpredicting the onset of flow separation. Nonetheless, this requires further investigation. The peak in the value of k at the inner wall is captured by all models. Although significantly underpredicted, the new model and the Lien NL $k-\varepsilon$ models return closer predictions to the experimental data compared to the other models. Unfortunately, there is no experimental data for the turbulent shear stress at this location to explore how turbulence anisotropy is predicted by the new model. However, it is encouraging that further downstream at $x/h = +2$, the turbulent kinetic energy, which has now diffused outwards in the inner half of the channel, is predicted well by the proposed model compared to the other models. This is shown in Figure 11 (b). The new model shows an important advantage in the prediction of the maxima here. This is echoed by a similar improvement of approximately 25% in the prediction of the peak value of the turbulent shear stress (Figure 12) compared to the standard $k-\omega$ model, which is also a 14% and 21% more accurate peak shear stress prediction compared to the Shih NL $k-\varepsilon$ and Lien NL $k-\varepsilon$ models, respectively.

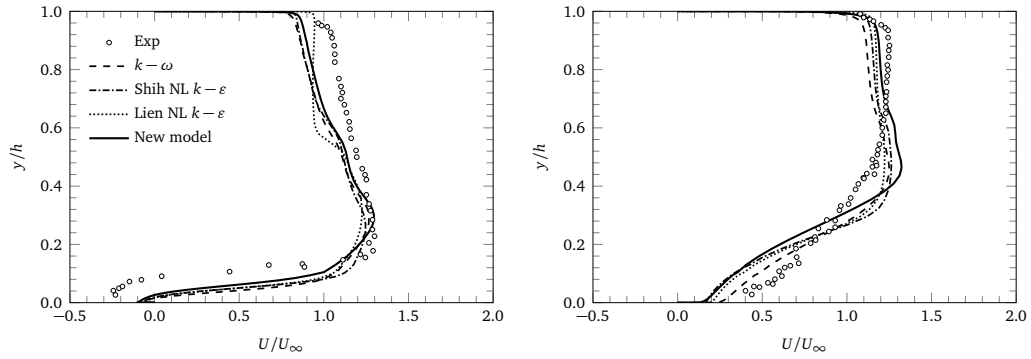

(a) $\theta = 180\,\text{deg}$ (b) $x/h = 2$

Figure 10: Longitudinal velocity profiles at two stations along the curved channel. Markers correspond to experimental data [70].

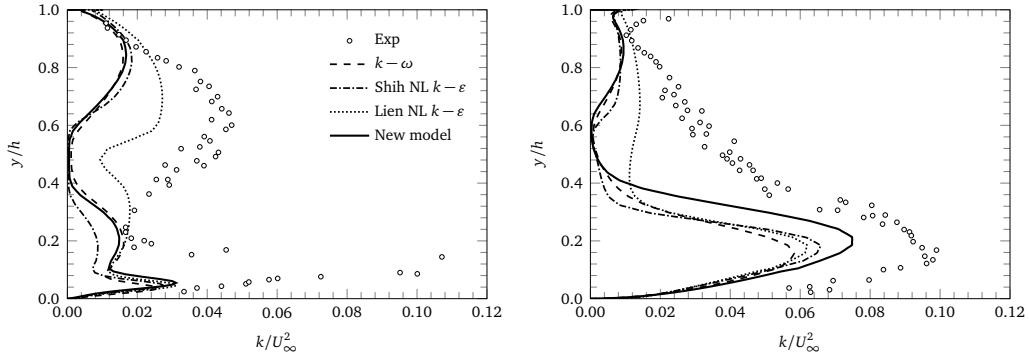

(a) $\theta = 180\,\text{deg}$ (b) $x/h = 2$

Figure 11: Turbulent kinetic energy profiles at two stations along the curved channel. Markers correspond to experimental data [70].

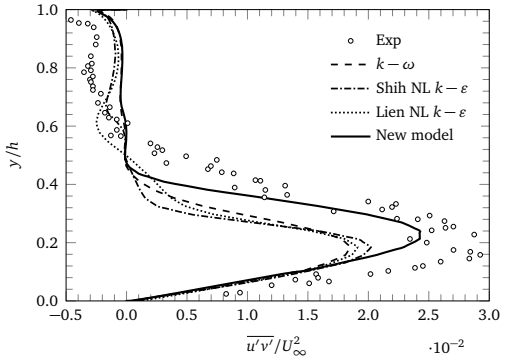

Figure 12: Turbulent shear stress at $x/h = 2$ along the curved channel. Markers correspond to experimental data [70].

The predictions for global quantities through the entire domain are illustrated through the skin friction and pressure coefficients at the outer and inner walls in Figures 13 and 14, respectively. They are plotted against the downstream distance, s, measured from the channel entrance on the centreline between the inner and outer walls and non-dimensionalised using h. The bend is located at $21.7 \leq s/h \leq 24.8$. These plots provide a means to assess of the performance of the new model.

From a practical engineering point of view, an accurate prediction of skin friction is important since heat transfer is proportional to skin friction whilst the prediction of pressure is important for measuring losses in the domain, for example due to curvature. In comparison to the experiment, the new model predicts the two quantities well upstream and through the bend. Downstream of the bend, at the location of minimum pressure on the outer wall where the flow accelerates, the new model predicts the pressure minima approximately 50% more accurately compared to the standard $k-\omega$ model and approximately 20% more accurately compared to the other non-linear models. This is accompanied by a prediction of the maxi-

mum skin friction coefficient within 1.5% of the experimental data, compared to the $k-\omega$ which underestimates it by 14%. The Shih NL $k-\varepsilon$ model also predicts this skin friction peak well, showing comparable prediction to the new model, while the Lien NL $k-\varepsilon$ model overpredicts it. Further downstream from the bend, the pressures on the inner and outer walls reach the same level at a value much lower than the upstream value, signifying pressure losses in the flow due to the curvature. The new model provides a 15% improvement compared to the standard $k-\omega$ model in the prediction of this pressure drop. As mentioned earlier, this has important practical implications. he Lien NL $k-\varepsilon$ model predicts a similar level of pressure coefficient in this region compared to the new model, although it overpredicts the skin friction coefficient here. The Shih NL $k-\varepsilon$ model returns comparable predictions to the standard $k-\omega$ model in terms of the pressure coefficients here, underpredicting the pressure drop through the bend.

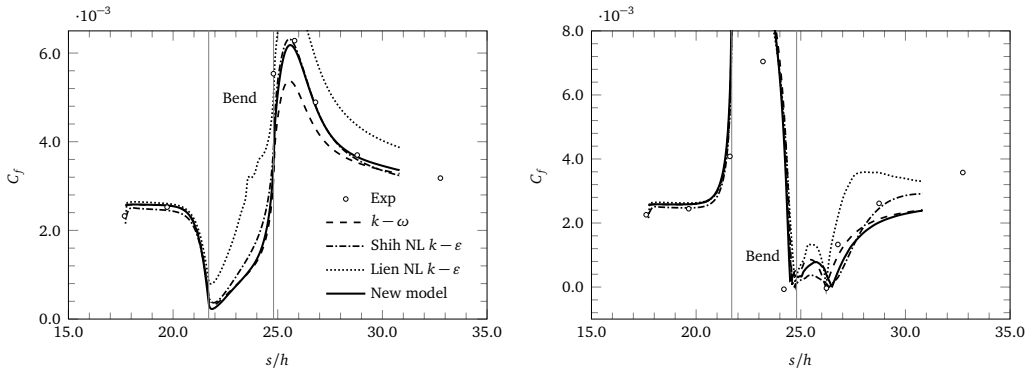

(a) Outer wall (b) Inner wall

Figure 13: Skin friction coefficient distribution of curved channel flow on the outer and inner walls. Markers correspond to experimental data [70].

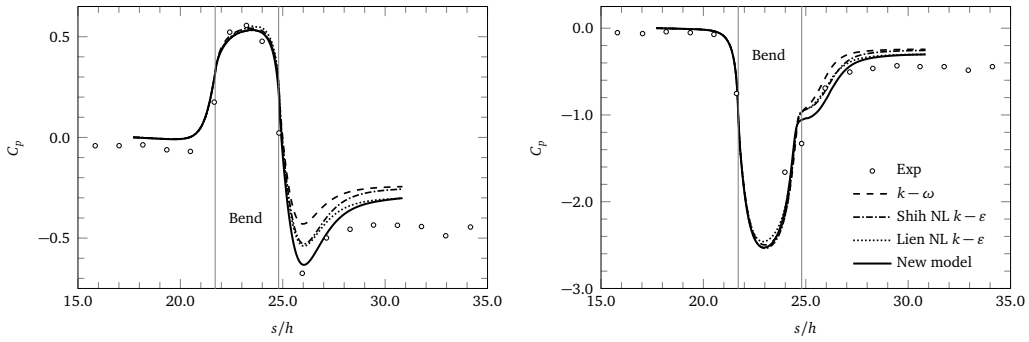

(a) Outer wall (b) Inner wall

Figure 14: Pressure coefficient distribution of curved channel flow on the outer and inner walls. Markers correspond to experimental data [70].

3.4. Planar diffuser with a downstream monolith

The new model is applied to a system consisting of a planar diffuser with a monolith downstream. The configuration tested here is based on one of the cases investigated experimentally and numerically by Porter et al. [73–75]. The geometry is presented in Figure 15. This configuration represents the setup of a simplified automotive exhaust catalyst system. An automotive catalytic converter uses a ceramic monolith consisting of many small parallel channels to provide a large surface area for the conversion of exhaust pollutants. The wide-angled diffuser, in this case 30 deg, is used to connect the inlet channel to the entrance of the monolith. This is a challenging case as the simulation should not only adequately capture flow separation in the diffuser, but also account for the pressure loss associated with the monolith itself. The Reynolds number of the case presented here is 2.2×10^4 based on the mean velocity and the hydraulic diameter of the nozzle upstream of the diffuser which is $D_h = 0.0384m$ in the experiment. The length of the monolith used here is $27mm$. The flow is modelled using a two-dimensional configuration with a symmetry boundary condition set along the x axis at centreline, $y = 0$, since the velocity profiles at the exit for various spanwise positions show symmetry and little variation in the experiment. The inlet turbulence intensity is set to 1% and the eddy viscosity ratio is 10. Grid independence is achieved by ensuring that the changes in the mean velocity and non-uniformity of the velocity profile near the outlet, as well as the pressure drop across the domain are sufficiently low (less than 2% here). This results in a hybrid grid consisting of 39,000 cells for the low-Re models. The corresponding maximum y^+ was 0.75. For the high-Re model, the grid consists of 28,000 cells. The corresponding maximum y^+ value was 7.1.

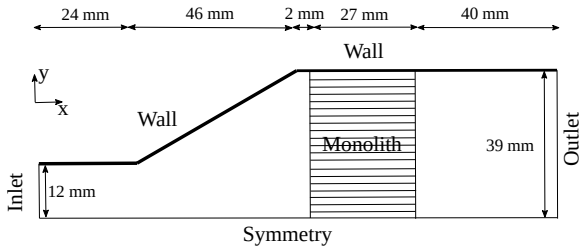

Figure 15: Computational domain of the planar diffuser case

There are a number of methods for modelling the monolith [73–75]. The approach used here is to treat the monolith as a porous medium with a prescribed resistance to reduce the computational effort. The resistance of the monolith is derived from the experimental measurements as discussed in [73] and fitted using the Darcy-Forchheimer equation which treats the porous zone as a sink term S_m in the momentum equation and is defined as:

$$S_m = -\left(\nu \mathbf{D} + \frac{1}{2}|U_{jj}|\mathbf{F} \right) U_i \tag{26}$$

where $\mathbf{D} = 3.96 \times 10^7/m^2$ and $\mathbf{F} = 23.74/m$, and the velocity used here is superficial velocity in the monolith. The turbulence quantities continue to be solved within the porous region using the default transport equations described by the turbulence model. The interface

between the fluid space and the porous region is treated using a boundary condition which sets the mean fields and turbulent quantities at the inlet of the monolith to be the same as the flow field immediately upstream of it.

The axial and transverse velocity profiles at 10.13 mm and 5.55 mm upstream of the monolith are shown in Figure 16. As the flow enters the diffuser, it essentially resembles a planar jet which impinges on the monolith. The flow turns transversely as it approaches the monolith. A portion of the flow is pushed through the monolith. The rest of the flow recirculates along the walls of the diffuser. This behaviour can be observed in Figure 16 (where the axial or transverse velocities are negative near the wall). The axial velocity profiles show that the predictions of the new model are generally in agreement with the experiment. Particularly, the predictions for the recirculation zone at $x = 5.55$ mm where the standard $k-\omega$ model fails to predict flow recirculation (i.e. the axial velocity component is positive). The proposed model returns a closer prediction to the experimental values in this recirculation region at 10.13 mm upstream compared to the other non-linear models, while the other non-linear models show closer predictions at 5.55 mm. As the flow gets closer to the monolith, the flow decelerates and spreads transversely. The proposed model shows an overall 20% improvement in the prediction of this the spreading when compared to the $k-\omega$ model which significantly overpredicts the distribution of the transverse velocity component. All the non-linear models show comparable predictions in the transverse velocity component at 10.13 mm, while the tested non-linear $k-\varepsilon$ models show an advantage over the proposed model at 5.55 mm where the new model overpredicts.

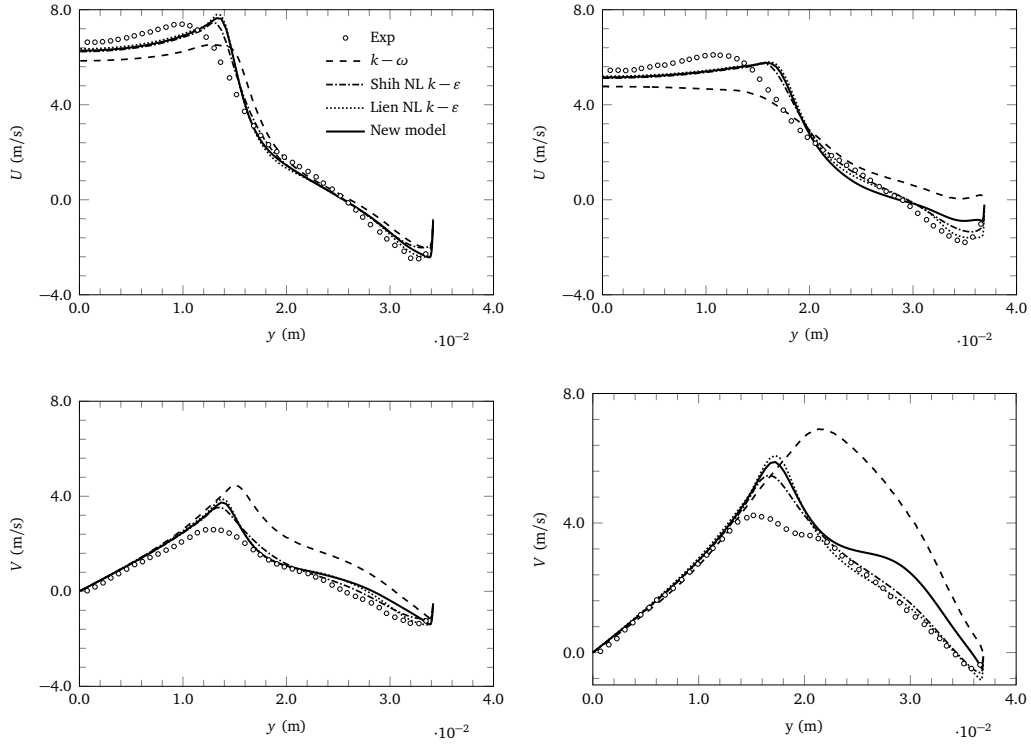

(a) 10.13mm upstream (b) 5.55mm upstream

Figure 16: Axial (U) and transverse (V) velocity profiles at two stations upstream of monolith. Markers correspond to experimental data [73].

This seemingly simple configuration involving a planar diffuser and a monolith results in complex flow interactions. The monolith affects the flow distribution within the diffuser, and in turn, the flow distribution upstream of the monolith dictates how it resists the flow. The practical consequence is that the flow through the monolith, and indeed, downstream is non-uniform or maldistributed, as shown in Figure 17. This figure shows the axial velocity profile at a downstream distance of 40 mm from the end of the monolith, normalised using the mean velocity. The new model shows a marked improvement compared to the $k-\omega$ by successfully capturing the maldistribution trend and the secondary peak near the wall in particular. Both of the tested non-linear $k-\varepsilon$ models also show the correct maldistribution trend here, returning comparable predictions to the proposed model, with the new model showing some advantage on the prediction of the secondary peak near the wall. Capturing this maldistribution correctly has important practical implications for the design of effective automotive after-treatment devices.

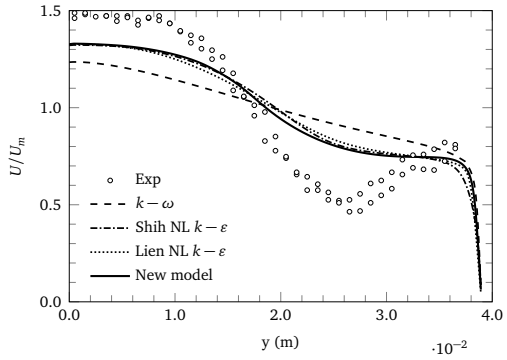

Figure 17: Axial velocity profile 40mm downstream of monolith. Markers correspond to experimental data [73].

3.5. Swirling flow

The model is now tested on a three-dimensional swirling flow configuration. The cases tested here were first investigated experimentally and numerically by Rusli et al. [76]. The geometry is shown in Figure 18, and includes: (i) a swirl generator with an annulus pipe, (ii) a sudden expansion diffuser, (iii) a monolith, and (iv) an outlet sleeve. For automotive applications, this simplified configuration can be used to study the influence that residual swirling flow from turbocharged engines have on the catalyst system. This configuration is also useful for assessing the performance of the proposed turbulence model on a three-dimensional application that involves rotational effects. The diffuser-monolith setup is similar to that presented in the previous section. However, the diffuser angle is 90 deg, i.e. a sudden expansion. The mass flow rate of the cases considered here is $63g/s$ and the mean velocity at the inlet is calculated based on the radius of the inlet channel, which is $0.022m$, and the fluid density, which is $1.18kg/m^3$ to match the experiments. Experimentally, the swirling inlet profile is produced by using a swirl generator. In order to match the experiment, it is included in the simulations. Two swirl generator angles are tested, 7 and 18 deg. As the swirl generator consists of 8 identical blocks spread azimuthally [77], a 45-deg wedge is used as the computational domain with periodic boundary conditions set on each side. The monolith is modelled using the porous medium approach and implemented as detailed in the previous section. Grid independence is achieved by monitoring the changes in the mean velocity, U_m, and swirl level, S (the definition of which is explained later) in the annulus, as well as the pressure drop, ΔP, across the domain. A summary of the grid independence test is presented in Table 3. The percentage of difference between the grids is calculated as $|f_1 - f_2|/f_1$ with f_1 representing the variable prediction of the finer mesh and f_2 is that of the coarser mesh. The 'Fine' mesh is chosen and it can be observed that the changes in the predicted variables between this mesh and the finer mesh is sufficiently low (around 2%). This results in a mesh consisting of polyhedral grid with a prism layer of 15 cells at the wall with a total of 2.7–3.0M cells. The corresponding maximum y^+ was 3.62.

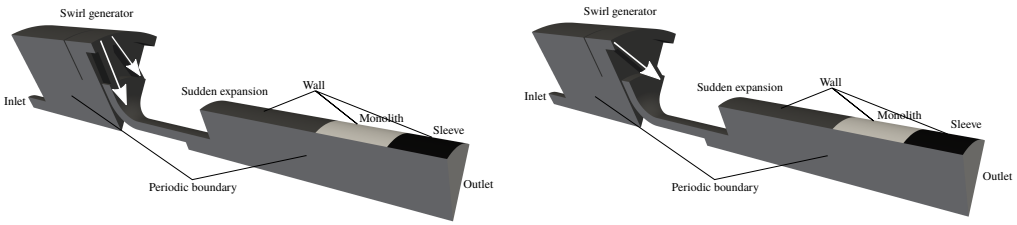

(a) Swirl generator angle = 7 deg (b) Swirl generator angle = 18 deg

Figure 18: Geometry of the swirling flow rig configuration at several swirl generator angles and swirl numbers.

Table 3: Summary of grid independence test for the swirling flow test case

	Number of cells	U_m $[m/s]$	% Diff U_m	ΔP $[Pa]$	% Diff ΔP	S	% Diff S
Very coarse	383,000	27.826	–	856.432	–	0.452	–
Coarse	1,210,000	27.742	0.30	822.570	4.11	0.445	1.57
Medium	1,790,000	27.751	0.03	816.988	0.68	0.448	0.67
Fine	3,000,000	27.738	0.05	804.341	1.57	0.449	0.22
Very fine	4,600,000	27.722	0.06	788.296	2.04	0.448	0.22

The swirl level produced by the swirl generator can be characterised by calculating a non-dimensional swirl number, S, within the annular extension that connects the outlet of the swirl generator to the sudden expansion diffuser. The swirl number is defined as:

$$S = \frac{G_\theta}{G_x r_o} \tag{27}$$

where G_θ and G_x are the tangential and axial momentum fluxes, respectively. They are given by:

$$G_\theta = \int_{r_i}^{r_o} \rho U W r 2\pi r dr \quad , \quad G_x = \int_{r_i}^{r_o} \rho U U 2\pi r dr \tag{28}$$

Here r is the radius of the annular channel from the centreline, r_i and r_o are the radii of the inner wall and the outer wall, respectively. The fluxes above are calculated from the axial and tangential velocity components in the annulus at a streamwise distance of 0.0775 m upstream of the expansion, which are shown in Figure 19. The calculated swirl numbers for the different swirl generator angles are presented in Table 4. Similar swirl numbers are predicted by the new model and the $k-\omega$ model. This allows a comparison of model predictions in the diffuser downstream. For convenience, the swirl number from the experiment is used for reference in the subsequent discussion.

Table 4: Summary of swirl number for swirling rig test case

Swirl generator angle	S (exp)	S $(k-\omega)$	S (new model)
7 (intermediate swirl)	0.44	0.43	0.42
18 (high swirl)	1.65	1.32	1.32

Figure 19 shows the velocities normalised using the mean axial velocity in the annulus, and plotted against r, the radial distance from the inner wall of the annulus, non-dimensionalised using r_o and r_i. The new model shows good agreement with the experiment for the axial velocity profile at $S = 0.44$ while the redistribution of the axial velocity at $S = 1.65$ is underpredicted. For the $S = 0.44$ case, the model shows improvement in the tangential velocity profile predictions while for the higher swirl level case both models do not capture the maximum value near the inner wall of the annular section. This can be attributed to a known weakness of the $k-\omega$ model for rotating flows, for example as observed in [78]. Some approaches to correct this behaviour have been proposed in literature, such as by including an explicit rotation correction term that uses non-inertial frames of reference, e.g. [36, 79]. This is not included in the present model since the focus of this work was to develop the non-linear formulation and the enhanced near-wall treatment for turbulence anisotropy.

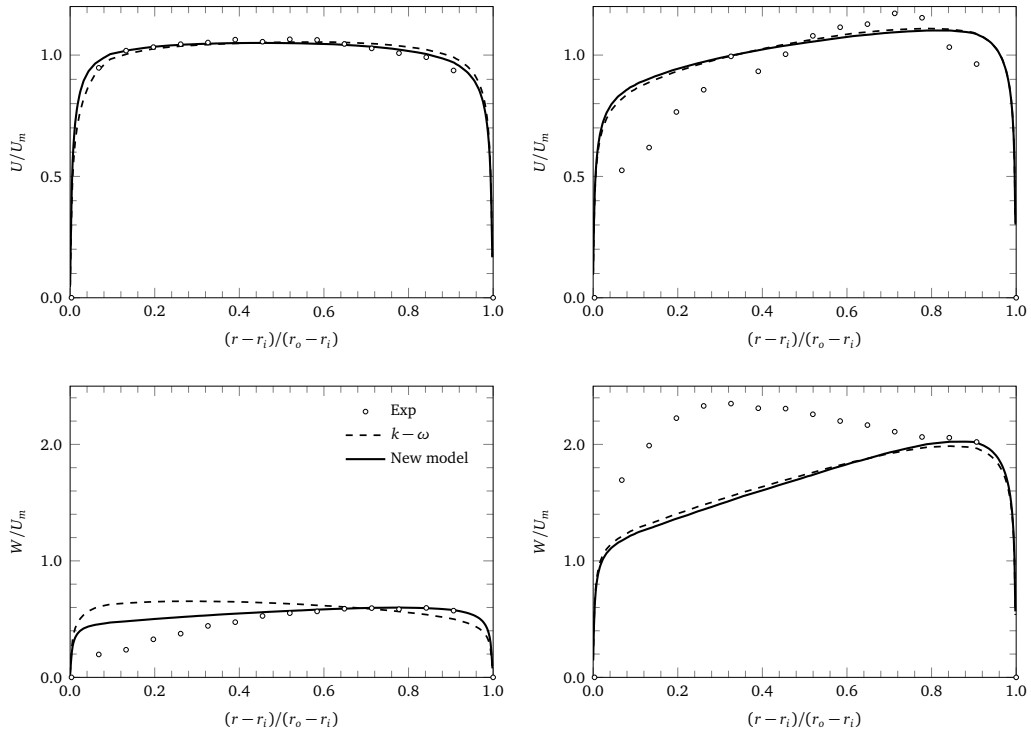

(a) $S = 0.44$ (b) $S = 1.65$

Figure 19: Mean axial (U) and tangential (W) velocity profiles within the annulus, at an axial distance of $0.0775m$ upstream of the expansion, at several swirl numbers. Markers correspond to experimental data [76].

The effect of swirl on the flow field within the diffuser can be examined through the pressure coefficient along the diffuser wall, as plotted in Figure 20 against the streamwise distance from the expansion. At both swirl levels, a decrease in pressure at the wall upstream of the expansion (for $-30 < x < 0$ mm) is shown in the experiment as the flow transitions from an annular cross-section to a circular cross-section. This trend is more pronounced at the higher swirl level, $S = 1.65$. The new model shows improvement in predicting this decrease in pressure compared to the $k-\omega$ model. At $S = 0.44$, as the flow enters the diffuser, there exists a recirculation region behind the expansion [76], which manifests as a drop in pressure along the wall. The pressure then recovers until the swirling jet reattaches at the wall which is marked by the pressure peak at the wall. The model predicts the extent of the recirculation zone and pressure level at the reattachment point well. At the higher swirl level, $S = 1.65$, the separated region behind the diffuser decreases in size and the flow stays attached along most of the diffuser wall, resulting in a "flatter" pressure coefficient profile. The profile and quantitative level predicted by the model closely matches the experiment in contrast to the $k-\omega$ model, which shows a more pronounced pressure variation along the wall.

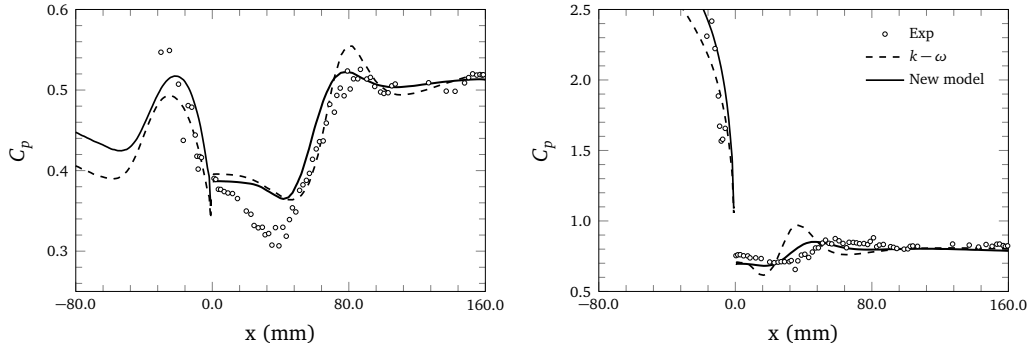

(a) $S = 0.44$ (b) $S = 1.65$

Figure 20: Pressure coefficient along the diffuser wall of the swirling flow setup at several swirl numbers. Markers correspond to experimental data [76].

4. Conclusion

This work introduced a new $k-\omega$ non-linear eddy-viscosity model in which the anisotropy tensor formulation for strain and rotation rates up to their quadratic level is retained. It is a non-linear extension of the classic $k-\omega$ model [45] with an added realisability condition. A new formulation for calculating the anisotropy expansion coefficients is proposed with focus on modelling the high level of turbulence anisotropy near the wall. Model predictions are validated and benchmarked against a range flow configurations involving boundary layers, curvature, separation, and swirl.

The proposed model correctly predicts a turbulent boundary layer in a zero-pressure-gradient flat plate test case, consistent with its formulation as a fully-turbulent model. The modification for enhanced treatment of near-wall turbulence anisotropy is shown to be efficient. In simple shear flow, compared to the baseline non-linear model, in which constant values are used, the near-wall modification improves the predicted Reynolds stress anisotropy by approximately 100%. In a curved channel flow, the model shows closer predictions to experimental data on the pressure and skin friction coefficients in general compared to the standard $k-\omega$ model as well as the other tested non-linear models, namely the Shih et al. quadratic $k-\varepsilon$ model [52] and the Lien et al. cubic $k-\varepsilon$ model [60]. In the acceleration region just downstream of the bend, the model produced improved predictions of the pressure minima of approximately 50% compared to the standard $k-\omega$ model, and approximately 20% more accurately compared to the other tested non-linear models. In a two-dimensional planar diffuser with a downstream monolith, the model shows good prediction of the flow maldistribution behind the monolith, successfully capturing the secondary velocity peak near the wall and returning comparable predictions to the other tested non-linear models. For a more complex configuration, involving a swirling flow case, the model predicts the pressure distribution along the diffuser wall closely matching the experimental data, showing improvement against the linear $k-\omega$ model on the swirl levels tested. The results obtained serve to showcase the capabilities of the new model for internal flows in particular. Specifically, they show the effectiveness of the proposed modification for predicting Reynolds stress anisotropy near the wall, which has been shown to be underpredicted by existing models,

e.g. [12, 42]. While there is some increase in the computation time by the proposed model in comparison with the standard $k-\omega$ model (around 12.8% for the more complex test case, which is the swirling flow case), the straightforward (and general) method for coupling the model with the underlying $k-\omega$ eddy-viscosity model, as well as the relative simplicity of the near-wall modification, opens a wealth of potential applications, particularly, since the modification relies only on local variables (in contrast to models that use wall-normal distance for example, e.g. [43]), which ensures its robustness for applications in complex geometries. The performance of the model for swirling flows could be improved by incorporating explicit corrections for flow rotation, such a modification will be the subject of future work.

[1] W. P. Jones, B. E. Launder, The prediction of laminarization with a two-equation model of turbulence, International journal of heat and mass transfer 15 (2) (1972) 301–314.

[2] A. K. Rastogi, W. Rodi, Calculation of general three-dimensional turbulent boundary layers, AIAA journal 16 (2) (1978) 151–159.

[3] N. C. G. Markatos, Transient flow and heat transfer of liquid sodium coolant in the outlet plenum of a fast nuclear reactor, International Journal of Heat and Mass Transfer 21 (12) (1978) 1565–1579.

[4] N. C. G. Markatos, M. R. Malin, G. Cox, Mathematical modelling of buoyancy-induced smoke flow in enclosures, International Journal of Heat and Mass Transfer 25 (1) (1982) 63–75.

[5] N. C. Markatos, K. A. Pericleous, An investigation of three-dimensional fires in enclosures, Fire Dynamics and Heat Transfer (1983) 115–124.

[6] N. C. G. Markatos, Hydrodynamics and heat transfer in enclosures containing a fire source, PCH Physico Chemical Hydrodynamics 5 (1) (1984) 53–66.

[7] C. G. Speziale, On turbulent secondary flows in pipes of noncircular cross-section, International Journal of Engineering Science 20 (7) (1982) 863–872.

[8] T. Von Karman, Some aspects of the turbulence problem, in: Proceeding of the 4th International Congress of Applied Mechanics, Cambridge, 1934, p. 54.

[9] J. Luo, B. Lakshminarayana, Prediction of strongly curved turbulent duct flows with reynolds stress model, AIAA journal 35 (1) (1997) 91–98.

[10] C. L. Rumsey, T. B. Gatski, J. H. Morrison, Turbulence model predictions of strongly curved flow in a u-duct, AIAA journal 38 (8) (2000) 1394–1402.

[11] J. P. Bertoglio, Homogeneous turbulent field within a rotating frame, AIAA Journal 20 (9) (1982) 1175–1181.

[12] T. J. Craft, B. E. Launder, K. Suga, Development and application of a cubic eddy-viscosity model of turbulence, International Journal of Heat and Fluid Flow 17 (2) (1996) 108–115.

[13] F. Schmitt, About boussinesq's turbulent viscosity hypothesis: historical remarks and a direct evaluation of its validity, Comptes Rendus Mecanique 335 (9) (2007) 617–627.

[14] S. B. Pope, Turbulent flows, Cambridge university press, 2000.

[15] J. C. Rotta, Statistische theorie nichthomogener turbulenz, Zeitschrift für Physik 129 (6) (1951) 547–572.

[16] J. L. Lumley, Toward a turbulent constitutive relation, Journal of Fluid Mechanics 41 (02) (1970) 413–434.

[17] S. B. Pope, A more general effective-viscosity hypothesis, Journal of Fluid Mechanics 72 (02) (1975) 331–340.

[18] B. E. Launder, Low-Reynolds number turbulence near walls, University of Manchester Institute of Science and Technology (UMIST) Department of Mechanical Engineering, 1986.

[19] P. A. Durbin, Near-wall turbulence closure modeling without "damping functions", Theoretical and Computational Fluid Dynamics 3 (1) (1991) 1–13.

[20] J. Kim, P. Moin, R. Moser, Turbulence statistics in fully developed channel flow at low reynolds number, Journal of fluid mechanics 177 (1987) 133–166.

[21] P. A. Durbin, Separated flow computations with the k-epsilon-v-squared model, AIAA Journal 33 (4) (1995) 659–664.

[22] R. N. Meroney, P. Bradshaw, Turbulent boundary-layer growth over a longitudinally curved surface, AIAA Journal 13 (11) (1975) 1448–1453.

[23] B. E. Launder, G. Reece, W. Rodi, Progress in the development of a reynolds-stress turbulence closure, Journal of fluid mechanics 68 (3) (1975) 537–566.

[24] W. Rodi, The prediction of free turbulent boundary layers by use of a two equation model of turbulence, Ph.D. thesis, Imperial College London (1972).

[25] W. Rodi, A new algebraic relation for calculating the reynolds stresses, in: Gesellschaft Angewandte Mathematik und Mechanik Workshop Paris France, Vol. 56, 1976, p. 219.

[26] D. D. Apsley, W.-L. Chen, M. Leschziner, F.-S. Lien, Non-linear eddy-viscosity modelling of separated flows, Journal of Hydraulic research 35 (6) (1997) 723–748.

[27] T. B. Gatski, T. Jongen, Nonlinear eddy viscosity and algebraic stress models for solving complex turbulent flows, Progress in Aerospace Sciences 36 (8) (2000) 655–682.
[28] T. B. Gatski, C. L. Rumsey, Linear and nonlinear eddy viscosity models, in: B. E. Launder, N. D. Sandham (Eds.), Closure strategies for turbulent and transitional flows, Cambridge University Press, 2002, Ch. 1, pp. 9–46.
[29] M. A. Leschziner, Modelling turbulent separated flow in the context of aerodynamic applications, Fluid dynamics research 38 (2) (2006) 174–210.
[30] A. Hellsten, S. Wallin, Explicit algebraic reynolds stress and non-linear eddy-viscosity models, International journal of computational fluid dynamics 23 (4) (2009) 349–361.
[31] S. Nisizima, A. Yoshizawa, Turbulent channel and couette flows using an anisotropic k-epsilon model, AIAA journal 25 (3) (1987) 414–420.
[32] C. G. Speziale, On nonlinear kl and k-ε models of turbulence, Journal of Fluid Mechanics 178 (1987) 459–475.
[33] T. J. Craft, B. E. Launder, K. Suga, Prediction of turbulent transitional phenomena with a nonlinear eddy-viscosity model, International Journal of Heat and Fluid Flow 18 (1) (1997) 15–28.
[34] K. Suga, K. Abe, Nonlinear eddy viscosity modelling for turbulence and heat transfer near wall and shear-free boundaries, International journal of heat and fluid flow 21 (1) (2000) 37–48.
[35] D. D. Apsley, M. A. Leschziner, A new low-reynolds-number nonlinear two-equation turbulence model for complex flows, International Journal of Heat and Fluid Flow 19 (3) (1998) 209–222.
[36] T. B. Gatski, C. G. Speziale, On explicit algebraic stress models for complex turbulent flows, Journal of fluid Mechanics 254 (1993) 59–78.
[37] S. Wallin, A new explicit algebraic reynolds stress turbulence model for 3d flows, in: Proceedings of the 11th Symposium on Turbulent Shear Flows, 1997, pp. 13.13–13.17.
[38] S. Wallin, A. V. Johansson, An explicit algebraic Reynolds stress model for incompressible and compressible turbulent flows, Journal of Fluid Mechanics 403 (2000) 89–132.
[39] P. G. Huang, P. Bradshaw, T. J. Coakley, Assessment of closure coefficients for compressible-flow turbulence models, Tech. rep., NASA (1992).
[40] D. C. Wilcox, Comparison of two-equation turbulence models for boundary layers with pressure gradient, AIAA journal 31 (8) (1993) 1414–1421.
[41] J. Larsson, Two-equation turbulence models for turbine blade heat transfer simulations, ISABE paper (1997) 97–7163.
[42] B. Song, R. S. Amano, G. R. Liu, On computations of complex turbulent flow by using nonlinear k-o model, Numerical Heat Transfer: Part B: Fundamentals 39 (5) (2001) 421–434.
[43] K. Abe, Y.-J. Jang, M. A. Leschziner, An investigation of wall-anisotropy expressions and length-scale equations for non-linear eddy-viscosity models, International Journal of Heat and Fluid Flow 24 (2) (2003) 181–198.
[44] T.-H. Shih, W. W. Liou, A. Shabbir, Z. Yang, J. Zhu, A new $k-\varepsilon$ eddy viscosity model for high reynolds number turbulent flows, Computers & Fluids 24 (3) (1995) 227–238.
[45] D. C. Wilcox, Reassessment of the scale-determining equation for advanced turbulence models, AIAA journal 26 (11) (1988) 1299–1310.
[46] A. J. M. Spencer, R. S. Rivlin, The theory of matrix polynomials and its application to the mechanics of isotropic continua, Archive for rational mechanics and analysis 2 (1) (1958) 309–336.
[47] A. J. M. Spencer, R. S. Rivlin, Further results in the theory of matrix polynomials, Archive for Rational Mechanics and Analysis 4 (1) (1959) 214–230.
[48] R. Rubinstein, J. M. Barton, Nonlinear reynolds stress models and the renormalization group, Physics of Fluids A: Fluid Dynamics (1989-1993) 2 (8) (1990) 1472–1476.
[49] F. R. Menter, Zonal two equation k-turbulence models for aerodynamic flows, AIAA paper 2906 (1993) 1993.
[50] F. R. Menter, Improved two-equation k-omega turbulence models for aerodynamic flows, NASA STI/Recon Technical Report N 93 (1992) 22809.
[51] I. Kimura, T. Hosoda, A non-linear k–ε model with realizability for prediction of flows around bluff bodies, International Journal for Numerical Methods in Fluids 42 (8) (2003) 813–837.
[52] T.-H. Shih, J. Zhu, J. L. Lumley, A realizable reynolds stress algebraic equation model, Tech. rep., NASA (1993).
[53] K. Abe, T. Kondoh, Y. Nagano, On reynolds-stress expressions and near-wall scaling parameters for predicting wall and homogeneous turbulent shear flows, International journal of heat and fluid flow 18 (3) (1997) 266–282.
[54] A. K. Hellsten, New advanced kw turbulence model for high-lift aerodynamics, AIAA journal 43 (9) (2005) 1857–1869.
[55] D. B. Taulbee, An improved algebraic reynolds stress model and corresponding nonlinear stress model, Physics of Fluids A: Fluid Dynamics 4 (11) (1992) 2555–2561.
[56] T.-H. Shih, J. L. Lumley, Remarks on turbulent constitutive relations, Mathematical and computer modelling 18 (2) (1993) 9–16.

[57] P. A. Durbin, B. A. Pettersson Reif, Statistical theory and modeling for turbulent flows, John Wiley & Sons, 2011.
[58] M. Lee, R. D. Moser, Direct numerical simulation of turbulent channel flow up to retau 5200, Journal of Fluid Mechanics 774 (2015) 395–415.
[59] H. K. Myong, N. Kasagi, A new approach to the improvement of k-ε turbulence model for wall-bounded shear flows, JSME international journal. Ser. 2, Fluids engineering, heat transfer, power, combustion, thermophysical properties 33 (1) (1990) 63–72.
[60] F. S. Lien, W. L. Chen, M. A. Leschziner, Low-reynolds-number eddy-viscosity modelling based on non-linear stress-strain/vorticity relations, in: Proceedings of 3rd Symposium on Engineering Turbulence Modelling and Measurement, 1996, 1996, pp. 91–100.
[61] T. O. Foundation, OpenFOAM v6 User Guide.
URL `https://cfd.direct/openfoam/user-guide`
[62] E. Robertson, V. Choudhury, S. Bhushan, D. K. Walters, Validation of openfoam numerical methods and turbulence models for incompressible bluff body flows, Computers & Fluids 123 (2015) 122–145.
[63] N. Ashton, V. Skaperdas, Verification and validation of openfoam for high-lift aircraft flows, Journal of Aircraft (2019) 1–17.
[64] H. Medina, A. Beechook, H. Fadhila, S. Aleksandrova, S. Benjamin, A novel laminar kinetic energy model for the prediction of pretransitional velocity fluctuations and boundary layer transition, International Journal of Heat and Fluid Flow 69 (2018) 150–163.
[65] T. Barth, D. Jespersen, The design and application of upwind schemes on unstructured meshes, in: 27th Aerospace sciences meeting, 1989, p. 366.
[66] S.-E. Kim, B. Makarov, C. D, A multi-dimensional linear reconstruction scheme for arbitrary unstructured grids, in: 16th AIAA Computational Fluid Dynamics Conference, 2003, p. 3990.
[67] J. Coupland, Ercoftac special interest group on laminar to turbulent transition and retransition, T3A and T3B Test Cases.
[68] R. Abid, Evaluation of two-equation turbulence models for predicting transitional flows, International Journal of Engineering Science 31 (6) (1993) 831–840.
[69] C. L. Rumsey, B. A. Pettersson Reif, T. B. Gatski, Arbitrary steady-state solutions with the k-epsilon model, AIAA journal 44 (7) (2006) 1586–1592.
[70] D. Monson, H. Seegmiller, P. McConnaughey, Comparison of experiment with calculations using curvature-correctedzero and two equation turbulence models for a two-dimensional u-duct, in: 21st Fluid Dynamics, Plasma Dynamics and Lasers Conference, 1990, p. 1484.
[71] D. Monson, H. Seegmiller, P. McConnaughey, Comparison of ldv measurements and navier-stokes solutions in a two-dimensional 180-degree turn-around duct, in: 27th Aerospace Sciences Meeting, 1989, p. 275.
[72] P. Bradshaw, Effects of streamline curvature on turbulent flow, Tech. rep., DTIC Document (1973).
[73] S. Porter, A. K. Mat Yamin, S. Aleksandrova, S. Benjamin, C. A. Roberts, J. Saul, An assessment of cfd applied to steady flow in a planar diffuser upstream of an automotive catalyst monolith, SAE International Journal of Engines 7 (4) (2014) 1697–1704.
[74] S. Porter, An assessment of cfd applied to a catalytic converter system with planar diffuser, Ph.D. thesis, Coventry University (2016).
[75] S. Porter, J. Saul, S. Aleksandrova, H. Medina, S. Benjamin, Hybrid flow modelling approach applied to automotive catalysts, Applied Mathematical Modelling 40 (19-20) (2016) 8435–8445.
[76] I. H. Rusli, S. Aleksandrova, H. Medina, S. F. Benjamin, The effect of swirl on the flow uniformity in automotive exhaust catalysts, Tech. rep., SAE Technical Paper (2017).
[77] W. Leuckel, Swirl intensities, swirl types and energy losses of different swirl generating devices, Tech. Rep. G02/a/16, IFRF (1967).
[78] F. J. Brandsma, J. C. Kok, H. S. Dol, A. Elsenaar, Leading edge vortex flow computations and comparison with dnw-hst wind tunnel data, Tech. rep., National Aerospace Laboratory NLR (2001).
[79] B. E. Launder, D. P. Tselepidakis, B. A. Younis, A second-moment closure study of rotating channel flow, Journal of Fluid Mechanics 183 (1987) 63–75.